Ship Technology Research
Schiffstechnik

ISSN: (Print) (Online) Journal homepage: https://www.tandfonline.com/loi/ystr20

Nonlinear seakeeping and hydroelasticity of ships using potential flow simulations

Heinrich Söding

To cite this article: Heinrich Söding (2023): Nonlinear seakeeping and hydroelasticity of ships using potential flow simulations, Ship Technology Research, DOI: 10.1080/09377255.2023.2180241

To link to this article: https://doi.org/10.1080/09377255.2023.2180241

SHIP TECHNOLOGY RESEARCH (SCHIFFSTECHNIK)
https://doi.org/10.1080/09377255.2023.2180241

Taylor & Francis
Taylor & Francis Group

OPEN ACCESS Check for updates

Nonlinear seakeeping and hydroelasticity of ships using potential flow simulations

Heinrich Söding

Department of Fluid Mechanics and Ship Theory, Technical University Hamburg, Germany

ABSTRACT
Accurate predictions of the behavior of ships in steep regular waves or in a natural seaway must take into account nonlinear wave responses, especially for roll motions, section moments, and hull vibration excitation. In contrast to CFD methods, here fully nonlinear seakeeping simulations are presented based on potential flow with empirical corrections. This reduces the computing effort by several orders of magnitude. Comparisons with other calculations and model experiments for benchmark cases show that the accuracy of the present method is not worse than that of the best other computations and model experiments. After about ten years of development, the method appears mature for routine applications. The source code of the program is available from the author if an adequate gift is donated to the Mèdecins Sans Frontières.

ARTICLE HISTORY
Received 5 January 2023
Accepted 8 February 2023

KEYWORDS
Seakeeping; springing; whipping; potential flow; simulation

1. Introduction

The behaviour of ships in a heavy seaway is predicted with various objectives. To name only the most important ones: The loads in hull cross sections are required for dimensioning the hull's longitudinal members like shell, deck and longitudinals. Accelerations are responsible for losses of deck containers and sea-sickness of passengers. Severe roll motions may also cause container losses, cargo damage and injuries of passengers and crew or even capsizing. Wave-induced drift forces often cause speed losses and may contribute to the inability of a ship to avoid stranding in heavy wind and seaway directed onshore.

To predict seakeeping of ships, strip methods (Korvin-Kroukovski and Jacobs, 1957, Bertram et al., 2006), Green function methods (Papanikolaou and Schellin, 1992, El Moctar et al., 2021), Rankine panel methods (Bertram, 1990, El Moctar et al., 2021) and CFD methods (Ferziger and Peric, 2008, El Moctar et al., 2021) are used; the former 3 either as frequency-domain methods (dealing with ships in regular waves followed by a statistical analysis for natural waves) or as simulations (modelling the motions over time), whereas in CFD, simulations are used nearly exclusively. Frequency-domain methods cannot deal accurately with responses depending nonlinearly on wave height; thus high accuracy of predictions requires simulations.

The method described here is aimed to predict ship motions and other wave responses with the same (high) accuracy as CFD methods also in steep waves or seaway where nonlinear responses are important, however with a computational effort which is smaller than in CFD methods by orders of magnitude. On a present-day standard PC, simulating a time interval T takes, typically, less than $10T$, thus allowing extended simulations. This is attained by using a Rankine source method, which simulates the water flow around the ship as a potential flow. Contrary to CFD methods, viscous forces and flow separations (e.g. at stern, rudder, bilge keels) cannot be modelled in detail by potential methods. However, because these details are not dominant in seakeeping, they are modelled in the present method by empirical approximations.

The present method satisfies the nonlinear boundary conditions of the flow potential on the body surface and on the water surface both at their actual positions. Compared to methods which take into account nonlinear effects only for the body boundary condition (Hachmann, 1986, van Walree et al., 2020), satisfying also the nonlinear free surface conditions involves additional difficulties, but appears important for the accuracy of results (El Moctar et al., 2021, chapter 15). A key to solving these difficulties was using the concept of the acceleration potential (Bandyk and Beck, 2011).

2. Computational method for a rigid hull

The method for rigid hulls is described in detail in Söding (2020), El Moctar et al. (2021); thus, only an overview is given here.

CONTACT Heinrich Söding h.soeding@gmx.de Technical University Hamburg, Johannes-Brahms-Str. 10, 21365, Germany
This article has been corrected with minor changes. These changes do not impact the academic content of the article.

The flow potential is determined by a panel method, here in the ‘patch method’ variant (Söding, 1993). On the body, the panel grid is generated once only before starting the simulation, separately for hull, possibly deck and superstructures (if these may become submerged during the simulation), and transom (Figure 1). Transom panels are assumed dry (skipped) or wet (taken into account) depending on the transom Froude number based on the actual flow speed at the transom and on its depth of the immersion (Mola et al., 2017). To apply a body-fixed panel mesh reduces the numerical effort of the simulation and improves the robustness of the method. It implies that there are partly immersed panels. The pressure force and moment on these panels are determined using only the submerged part. Further, the influence of partly submerged panels on the flow potential is reduced according to the ratio α of submerged to total panel area. This is accomplished by multiplying the coefficient on the main diagonal of the equation system for source strengths, which corresponds to that panel, by the factor $1/\alpha$.

If non-smooth body parts like superstructures, containers etc. become submerged, potential flow cannot resolve the massive flow separation at these obstacles, especially in case of substantial forward speed. Thus the accuracy of results will suffer, but the simulation can proceed also in these cases.

In most (even linear) panel methods, second derivatives of the flow potential at the hull surface are required. These may cause accuracy problems because typical panel methods converge for small panel size to correct first, but not to correct second derivatives of the potential. In the present method, however, second derivatives of the potential are required only for the incident waves (where they can be computed accurately), not for the flow disturbance by the body, because the latter is formulated as following the body motions, an idea taken from Hachmann (1991).

The wave field around the body consists of

(1) An incident regular wave, or a stationary incident natural seaway
(2) Waves generated by the mean forward speed of the ship (below called steady waves)
(3) Radiation waves generated by the oscillatory ship motions
(4) Diffraction waves consisting of reflections of incident waves at the ship hull and waves transmitted under the hull to its lee side

The nonlinear interactions between these contributions are taken into account. In the following, waves listed under 2 to 4 will collectively be called disturbance waves.

Rankine sources for modelling the water flow around the ship require a panel mesh also on the water surface. The alternative of using Green functions which satisfy also the linearized free-surface condition is not used here because it can satisfy neither the interaction with the steady flow around the ship in case of forward speed, nor the nonlinear free-surface boundary conditions. High accuracy requires that the free surface panel mesh may not be extended into the ship hull; instead, it must be generated around the actual waterline, and it must reach up to a suitable distance from the body. The radiation condition (steady waves not in front of the body; only outgoing radiation and diffraction waves) is satisfied best in a structured panel mesh. Because the waterline shape may change severely, for example, if a transom changes from immersed to emerged, the free-surface panel mesh is generated anew at the beginning of each time step. Within each time step, the mesh is deformed, keeping its topology. The Runge–Kutta 4th order method is applied for time integration; it implies four sub-steps per time step.

Reflections of disturbance waves at the outer boundary of the free-surface panel mesh must be avoided. This is alleviated by computing only the disturbance waves numerically by means of the panel method, and by damping them, assuming higher or lower atmospheric pressure where the water surface is moving (in a coordinate system moving with the horizontal ship velocity) upward or downward, respectively. The applied damping factor is small at the waterline and increases gradually farther off from the body.

Excitations by regular waves or a natural seaway are determined, however, without any damping. Nonlinear regular waves are determined using Fenton’s method (Fenton,2018). It uses a Fourier development of the stream function of the wave flow and a modified Newton method for solving numerically a nonlinear equation system for the Fourier coefficients and some other quantities. The equations of this system follow from continuity and the nonlinear boundary conditions at the water surface. Deep or shallow water may be prescribed.

To simulate the ship in a natural seaway, a linear superposition of regular (elementary) waves of different frequency and direction (the latter only in case of short-crested seaway) is used. Because short waves have not much influence on ship motions and loads, the wave spectrum is approximated only up to a maximum frequency of 2.5 times the peak frequency. For the same reason, a high-order approximation of the natural seaway (e.g. Ducrozet et al., 2016) is held to be unnecessary here. However, the most important nonlinear effects in a seaway are taken into account approximately by evaluating the wave flow potential of the elementary waves, as well as its partial

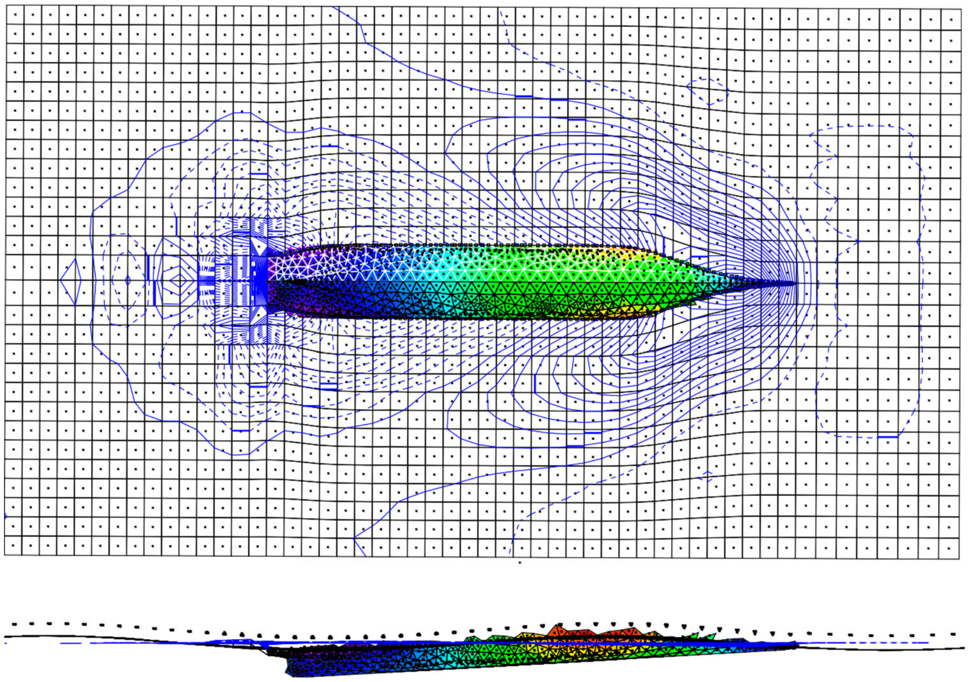

Figure 1. Example of a panel mesh of the 6500 TEU containership in regular head waves of 8 m height. Point sources are indicated as dots. Colors on hull panels code the dynamic pressure, contour lines show the disturbance waves. Slight differences between port and starboard waves are caused by minor programming details involving the order of panels.

derivatives, at the actual point of interest, for example, at the actual, not the mean water surface. However, this requires special precautions. Without these, short elementary waves would become overly steep on the wave crests of the total seaway, and would nearly vanish in its wave troughs, due to the factor $\exp(-kz)$ (for z increasing downwards), which, for short waves (large wave number $k = 2\pi/\lambda$, where λ is the wave length), may be $>> 1$ on a wave crest, or nearly 0 in a wave trough.

In the relevant literature (e.g. El Moctar et al., 2021, chapter 4), several methods are described to better approximate the nonlinear seaway. In the present programme, to determine wave flow quantities at a point $\vec{x}$, at first the 'orbital motion centre' $\vec{x}_0$ is determined, at which the fluid particle would come to rest if the seaway were fading out. The interesting flow properties are then determined as a sum over all elementary waves. For each elementary wave e, flow quantities are then evaluated at a point $\vec{x}_e$ between $\vec{x}$ and $\vec{x}_0$, where $\vec{x}_e - \vec{x}_0$ takes account of all waves with wave number $k \geq k_e$, but excluding those with $k < k_e$.

To satisfy the radiation condition for the steady waves, Dawson's method (Dawson,1977) is used: Derivatives of the disturbance wave potential in the direction of the steady flow at a point P are determined numerically using 4 points at and in front of P. The coefficients of the formula are determined from approximating the potential by a 4th-order polynomial lacking the 3rd-order term.

The flow potential of the incident wave or seaway is known primarily at the surface of the incident waves and must be continued to the surface of the combined incident and disturbance waves. This may cause instabilities of the procedure to satisfy the nonlinear free-surface conditions. Means to avoid this are described in Söding (2020).

A look to the waterline of a ship with reasonable forward speed shows that there is no smooth, sharp water surface. Therefore, in the present method the surface height and the flow features at the waterline are determined not from the body and/or free-surface boundary conditions, but are extrapolated from the next two grid points aside. Correspondingly, decreasing the free-surface panel sizes too much, especially in case of high Froude numbers, will result in too steep disturbance waves, causing divergence and stopping the simulation.

Modern cargo ships have, typically, strongly flaring or nearly flat section shapes above the propeller and rudder. This may cause a dove-tail shaped or even discontinuous waterline at the stern, resulting in a rugged free-surface panel mesh. To avoid this, the least-squares method is applied in each time step to approximate the waterline in the stern region of such ships by a straight line.

The boundary condition at the water surface contains terms involving the partial time derivative of the flow potential. To determine the latter from finite differences between successive time steps would be inaccurate because the panel mesh may change even topologically. Therefore, the time derivatives are determined directly from time derivatives of the boundary conditions (Bandyk and Beck,2011).

However, interpolation of flow quantities between different panel meshes at the end of one time step and the beginning of the next one is still necessary for the water surface height and the disturbance flow potential there.

In every time sub-step, eight linear equation systems are solved for the source strengths belonging to each panel. One system follows from the boundary conditions of the flow potential, six follow from the time derivatives of the body boundary conditions for unit accelerations of the body in its six degrees of freedom (these are used to determine the added mass matrix of the body), and one for the time derivative of that part of the flow potential which does not depend on the body accelerations. Because these eight linear equation systems have the same coefficient matrix, their solution does not require substantially more computer time than solving a single equation system.

To use the added mass matrix for the time integration of the body motions improves substantially its stability and accuracy and allows relatively large time steps (Söding,2001). Typically 25 to 35 time steps per wave encounter period are used in the Runge–Kutta time integration, which determines the following time functions:

Average potential on each free-surface panel
Free-surface height at panel corners
Three components of translation of the ship's centre of gravity and of its translation speed
Three Euler angles and three components of the angular velocity of ship rotation

The transverse 'lift' force generated by the hull and the rudder (in midship position) in case of a drift angle or oblique waves cannot be determined directly by a source-generated potential flow. Instead, it is estimated by a formula following from slender-body theory (Brix,1993).

In the following, only straight-ahead courses are simulated. The ship should then keep, on a longer time scale, the prescribed speed, course angle and track while allowing wave-induced ship motions in all degrees of freedom. This is accomplished, like in many model experiments, by applying external longitudinal and transverse forces and a yaw moment. Their size is determined by a PID controller depending on the deviation of ship position and heading from the intended values.

To avoid excessive pressure and surface deformation at the start of a simulation, the ship is accelerated from zero speed to the intended average speed, using an acceleration decreasing linearly to zero within a given time interval.

3. Hull vibrations

Loads in transverse ship sections may be substantially influenced by wave-induced hull vibrations. Therefore the programme was extended to take account of global hull vibrations, in which the ship's cross sections translate and rotate, but do not deform.

Typically, the lowest eigenfrequency of hull vibrations is 5–10 times larger than the encounter frequency of the most relevant head waves. To treat these vibrations like the rigid-body motions by integrating their motion equations numerically would require five to ten times smaller time steps even if only the lowest vibration mode is taken into account. To avoid this increase in computing time, only the vibration excitation is treated nonlinearly, while hull vibrations following from that excitation are determined using a linear method. This is possible because global hull vibrations have amplitudes which are, even in large ships, typically less than 5% of the exciting wave amplitude. Further, the nonlinear vibration excitation can be determined for the rigid hull without knowing its vibrations. This allows to determine the vibrations using time steps which are not substantially smaller then required to simulate motions of the rigid hull.

A modal analysis of global hull deformations is performed by a separate program [Söding 2009] before starting the simulation. In the examples described later, the hull was modelled simply as a Timoshenko beam, taking into account only vertical bending and shear deformation. According to various full-scale measurements, for example, Mathisen et al. (2009), these vertical, symmetric vibrations contribute much more to the vibration amplitudes than coupled horizontal/torsional and longitudinal vibrations. Six modes of lowest eigenfrequency were taken into account. They have two to seven nodes (zero points of the oscillatory mode shape).

Determining the mode frequencies and mode shapes in still water before starting the simulation avoids to increase the required computing time compared to rigid-body simulations; however, this neglects the change of eigenfrequencies (and slight changes of the mode shapes) caused by the added mass, which depends on the submergence especially of both ship ends. At the moment, there is no proof that this has only small influence on the loads in hull cross sections, but it is estimated as plausible.

The following data are determined for the selected number of modes and transferred to the simulation programme:

Mode eigenfrequency Ω and damping. The latter is estimated only from full-scale measurements in similar ships.
Mode shapes described by the translation and rotation of cross sections at a number of longitudinal

positions. Between these, the mode shape is interpolated.

Additional loads caused by the modal vibration at those cross sections where shear force and bending moment are of interest, separately for unit modal deformation and unit acceleration (Damping forces are much smaller and are neglected here).

Vibratory translations $\vec{U}(x, t)$ of the ship's cross sections at the ship-fixed longitudinal position x are approximated as

$$\vec{U}(x, t) = \sum_{j=1}^{J} v_j(t)\vec{u}(x), \tag{1}$$

where $\vec{u}(x)$ is the translational mode shape, and J is the number of modes taken into account. As the different modes are uncoupled by definition, each mode is considered separately. Therefore, the index j is omitted in the following. The time function $v(t)$ follows from the motion equation

$$kv(t) + \mathrm{d}\dot{v}(t) + m\ddot{v}(t) = f(t). \tag{2}$$

Modal stiffness k, damping d and mass m follow from the modal analysis and are approximated as constant during the simulation. Only the mode excitation $f(t)$ and the vibration $v(t)$ following from it must be determined during the simulation. The excitation is

$$f(t) = \int_L \vec{q}(x)\vec{u}(x)\mathrm{d}x. \tag{3}$$

Here $\vec{q}$ is the external pressure load per unit length in x direction together with the d'Alembert mass load produced by the rigid-body accelerations.

At the beginning (designated by index 1) of each Runge–Kutta time step of length Δt, the quantities v_1, $\dot{v}_1$ and $\ddot{v}_1$ are known as results of the previous time step. At time $\Delta t/2$ later, the excitation f_2 is determined as the average result of Equation (3) for the second and third Runge–Kutta sub-steps; and at the end of the time step, f_3 is determined for the first sub-step of the next time step. From these quantities, v_3, $\dot{v}_3$ and $\ddot{v}_3$ at the end of the time step shall be determined, together with intermediate results v_2, $\dot{v}_2$ and $\ddot{v}_2$ at the middle of the time step.

From Equation (2) follows:

$$kv_2 + \mathrm{d}\dot{v}_2 + m\ddot{v}_2 = f_2; \tag{4}$$

$$kv_3 + \mathrm{d}\dot{v}_3 + m\ddot{v}_3 = f_3. \tag{5}$$

The vibration acceleration $\ddot{v}(t)$ is approximated as a second-order polynomial having the values $\ddot{v}_1$, $\ddot{v}_2$ and $\ddot{v}_3$ at times t_1, $t_1 + \Delta t/2$ and $t_1 + \Delta t$, respectively:

$$\ddot{v}(t) = \ddot{v}_1 + (-3\ddot{v}_1 + 4\ddot{v}_2 - \ddot{v}_3)\frac{t - t_1}{\Delta t} + (2\ddot{v}_1 - 4\ddot{v}_2 + 2\ddot{v}_3)\frac{(t - t_1)^2}{(\Delta t)^2}. \tag{6}$$

Integrating this equation gives

$$\begin{aligned}\dot{v}(t) &= \dot{v}_1 + \int_0^{t-t_1} \ddot{v}(t_1 + \tau)\mathrm{d}\tau \\ &= \dot{v}_1 + \ddot{v}_1(t - t_1) + (-3\ddot{v}_1 + 4\ddot{v}_2 \\ &\quad - \ddot{v}_3)\frac{(t - t_1)^2}{2\Delta t} + (2\ddot{v}_1 - 4\ddot{v}_2 \\ &\quad + 2\ddot{v}_3)\frac{(t - t_1)^3}{3(\Delta t)^2}.\end{aligned} \tag{7}$$

Another integration results in

$$\begin{aligned}v(t) &= v_1 + \int_0^{t-t_1} \dot{v}(t_1 + \tau)\mathrm{d}\tau \\ &= v_1 + \dot{v}_1(t - t_1) + \ddot{v}_1\frac{(t - t_1)^2}{2} \\ &\quad + (-3\ddot{v}_1 + 4\ddot{v}_2 - \ddot{v}_3)\frac{(t - t_1)^3}{6\Delta t} \\ &\quad + (2\ddot{v}_1 - 4\ddot{v}_2 + 2\ddot{v}_3)\frac{(t - t_1)^4}{12(\Delta t)^2}.\end{aligned} \tag{8}$$

From Equation (7), the following two equations result for $t = t_1 + \Delta t/2$ and $t = t_1 + \Delta t$, respectively:

$$\dot{v}_2 = \dot{v}_1 + (5\ddot{v}_1 + 8\ddot{v}_2 - \ddot{v}_3)\frac{\Delta t}{24}; \tag{9}$$

$$\dot{v}_3 = \dot{v}_1 + (\ddot{v}_1 + 4\ddot{v}_2 + \ddot{v}_3)\frac{\Delta t}{6}. \tag{10}$$

Correspondingly, Equation (8) results in the relations

$$v_2 = v_1 + \dot{v}_1\frac{\Delta t}{2} + (7\ddot{v}_1 + 6\ddot{v}_2 - \ddot{v}_3)\frac{(\Delta t)^2}{96}; \tag{11}$$

$$v_3 = v_1 + \dot{v}_1\Delta t + (\ddot{v}_1 + 2\ddot{v}_2)\frac{(\Delta t)^2}{6}. \tag{12}$$

Equations (11), (9) and (4) are combined to eliminate v_2 and $\dot{v}_2$; correspondingly, v_3 and $\dot{v}_3$ are eliminated from a combination of Equation (12), (10) and (5). This results in a linear equation system of only 2 equations:

$$\begin{pmatrix} m + k(\Delta t)^2/16 + \mathrm{d}\Delta t/3 & -k(\Delta t)^2/96 - \mathrm{d}\Delta t/24 \\ k(\Delta t)^2/3 + 2\mathrm{d}\Delta t/3 & m + \mathrm{d}\Delta t/6 \end{pmatrix}\begin{pmatrix}\ddot{v}_2 \\ \ddot{v}_3\end{pmatrix} = \begin{pmatrix} f_2 - k(v_1 + \dot{v}_1\Delta t/2 + 7\ddot{v}_1(\Delta t)^2/96) - d(\dot{v}_1 + 5\ddot{v}_1\Delta t/24) \\ f_3 - k(v_1 + \dot{v}_1\Delta t + \ddot{v}_1(\Delta t)^2/6) - d(\dot{v}_1 + \ddot{v}_1\Delta t/6) \end{pmatrix} \tag{13}$$

This system is solved for $\ddot{v}_2$ and $\ddot{v}_3$. Equations (12) and (10) are then used to determine v_3 and $\dot{v}_3$, which become the values v_1 and $\dot{v}_1$ for the next time step. And if required, v_2 and $\dot{v}_2$ can be determined from Equations (11) and (9).

This procedure turns out to be slightly unstable if the non-dimensional vibration damping

$$D = \frac{d}{2m\Omega} \tag{14}$$

is zero or small, where $\Omega = \sqrt{k/m}$ is the mode eigenfrequency. Therefore, a small additional damping is added. Its non-dimensional parameter D_a is determined from the condition that the integration is stable, but near to the stability limit if the physical damping D is zero. The necessary additional damping depends on $\Omega\Delta t$; it is approximated here as

$$D_a = \exp\left(-3.1 - 0.81 \cdot \mathrm{Max}(3 - \Omega\Delta t,\ 0)^2\right). \tag{15}$$

Figure 2 illustrates this function.

For a typical case (large containership in a regular head wave with wave length $\lambda = 0.53L_{pp}$), this results in D_a values according to Table 1. In no case higher additional damping than 4.5% is required. In the usually more important cases of longer waves, D_a is even smaller than according to the above table. Thus, this integration scheme can be used for time steps exceeding one half of the shortest modal period without becoming unstable or giving unreasonable results.

4. Details of the following simulations

The number of Runge–Kutta time steps (each comprising four flow evaluations) was, usually, about 35 per wave encounter period. The number of panels on both sides of the ship hull varied between about 1900 and 4000, of which, typically, 55–60% are partly or fully submerged on average. The smaller number of body panels was shown to be sufficient even in the shortest waves tested. If large roll angles occur, additional panels are arranged on the ship's deck, and for low or zero ship speed also on the transom.

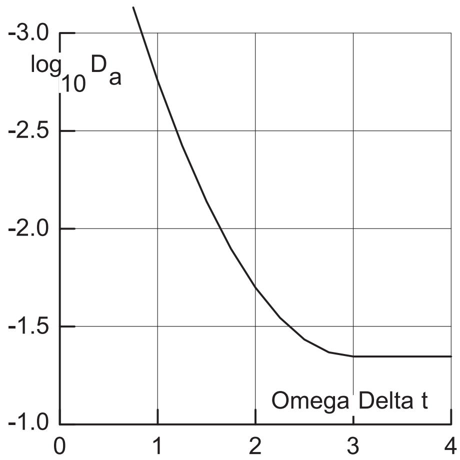

Figure 2. Additional non-dimensional damping D_a depending on time step Δt and mode eigenfrequency Ω.

Table 1. Additional non-dimensional damping D_a for six vertical vibration modes of a containership.

Mode	1	2	3	4	5	6
Ω [rad/s]	2.70	5.12	7.62	10.13	12.42	14.89
$\Omega\Delta t$	0.59	1.13	1.68	2.23	2.73	3.28
D_a	0.04%	0.26%	1.09%	2.78%	4.25%	4.50%

The typical panel size on the free surface was wave length (significant wave length in case of natural seaway) divided by 30–40, but not less than 5.5% of the ship length. This results in about 1200 free-surface panels in longer waves, and up to about 5000 in short waves.

Computing times are, typically, 7–10 times the simulated time span for large ships in full scale on a modern PC containing 10 real and 10 virtual processors. The programme is written in Fortran 95 with parallelization using OpenMP and linear algebra operations using LAPACK.

In the following, results for the three containerships of Table 2 will be presented.

Coordinates used in the following are x (positive forward), y (positive to starboard) and z (positive downward).

5. Verification for rigid ship hulls in regular head waves

Figures 3 and 4 show wave responses depending on wave frequency for the 10,000 TEU containership. Results of model experiments in regular waves of 3 m height by [Hong 2013] (Δ) are compared with results computed by [Oberhagemann 2016] using the RANSE commercial programme COMET ($\bullet$), with the linear panel method GLRankine (Söding et al., 2012; curves), and with the present method designated as SIS (Ship In a Seaway) ($\circ$ and $\star$). Generally, the motions determined by all these methods coincide quite well. An exception is the heave motion at low frequencies, where the linear programme GLRankine gives higher values than all other methods. In this frequency region, the heave motion is quite sensitive because in this frequency range is the heave resonance, where mass and restoring forces cancel, and also the Froude-Krilow excitation is largely cancelled by the diffraction force. Tests with different panel meshes for the GLRankine method show that the finite size of the panels is not responsible for this difference.

Table 2. Main particulars of the three containerships used as test cases.

	L_{pp}[m]	B[m]	T[m]	Δ[m^3]	x_G[m]	$r_{G,y}$[m]
10 000 TEU	321.0	48.4	15.00	142158	−9.00	77.22
6500 TEU	286.3	40.3	13.26	92952	−6.89	68.88
DTC	355.0	51.0	14.50	173467	−3.43	88.77

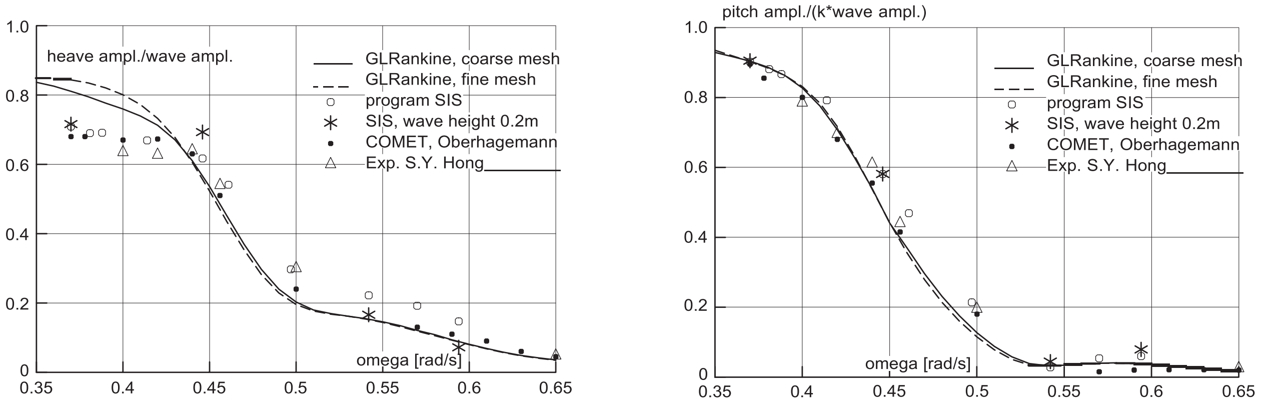

Figure 3. Nondimensional heave and pitch motion amplitudes at the centre of gravity *G* in periodical head waves of 3 m (asterisks: 0.2 m) height. 10,000 TEU containership at speed 20 kn. SIS: results of the present method.

More important is the finite wave height of 3 m, whereas GLRankine computes for a wave height tending to zero. The influence of this difference is illustrated by the circle (for 3 m) and asterisk (for 0.2 m wave height) symbols. The non-dimensional heave and pitch motions tend to 1 for low frequency, but this is not clearly visible in Figure 3 because the lowest frequency $\omega = 0.35$ rad/s shown in these figures is not small enough.

In Figure 4 the non-dimensional vertical bending moment at midship section is given, again as a function of wave frequency. Also here, differences between the different methods for 3m wave amplitude are quite small, whereas differences between 3m and vanishing wave amplitude are much larger.

In Figure 5, the dependence of the nondimensional responses on wave height is shown for a wide range of wave heights for a single wave length 310 m. The line to the point for 9 m wave height is broken because, in that condition, the ship's deck is partly submerged.

The following figures refer to the 6500 TEU containership. Figure 6 gives nondimensional linear transfer functions of surge, heave and pitch motions at the centre of gravity *G*, while Figure 7 shows transfer functions of the vertical shear force at $L_{pp}/4$ and $3L_{pp}/4$ before the aft perpendicular, and of the vertical bending moment M_y at midship section. Simulations using the present method were performed in waves of 1 m height using larger and smaller control forces (larger, smaller circles). Here, the results are sensitive to the size of the control force for heave and pitch at speed 15 knots near the wave frequency 0.5 rad/s. As before, the high sensitivity is caused by heave and pitch motion resonance and nearly cancelling of Froude–Krilow and diffraction excitation force. The substantial differences of the shear force shown in Figure 7 for higher frequencies between, on the one

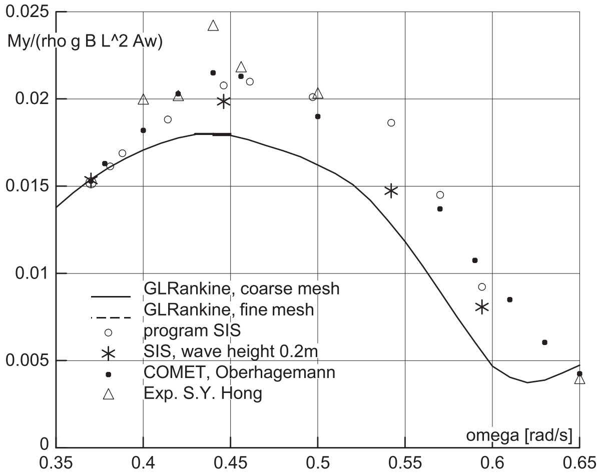

Figure 4. Nondimensional vertical midship bending moment amplitude. *ρ* means fluid density, *g* gravity acceleration, *L* ship length between perperdiculars, and A_w waterline area. Other details like in Figure 3.

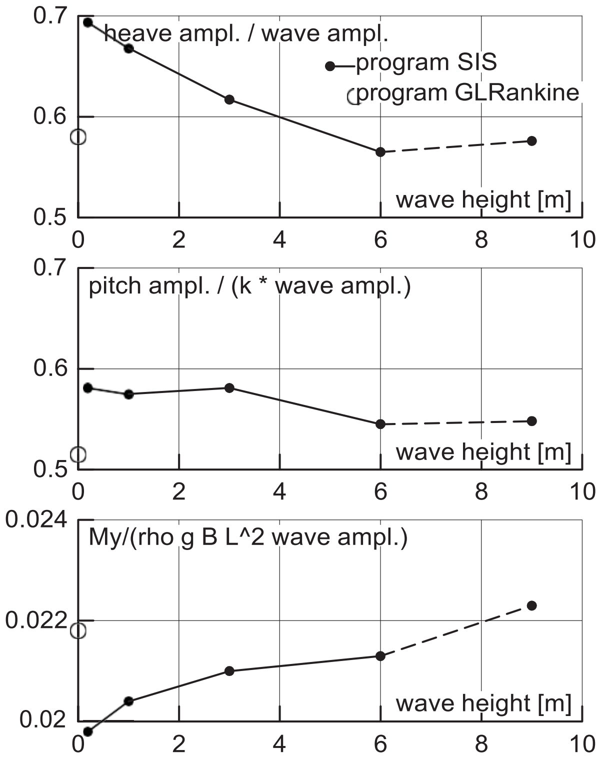

Figure 5. Dependence of nondimensional responses on wave height for wave length 310 m. Other details like in Figure 3.

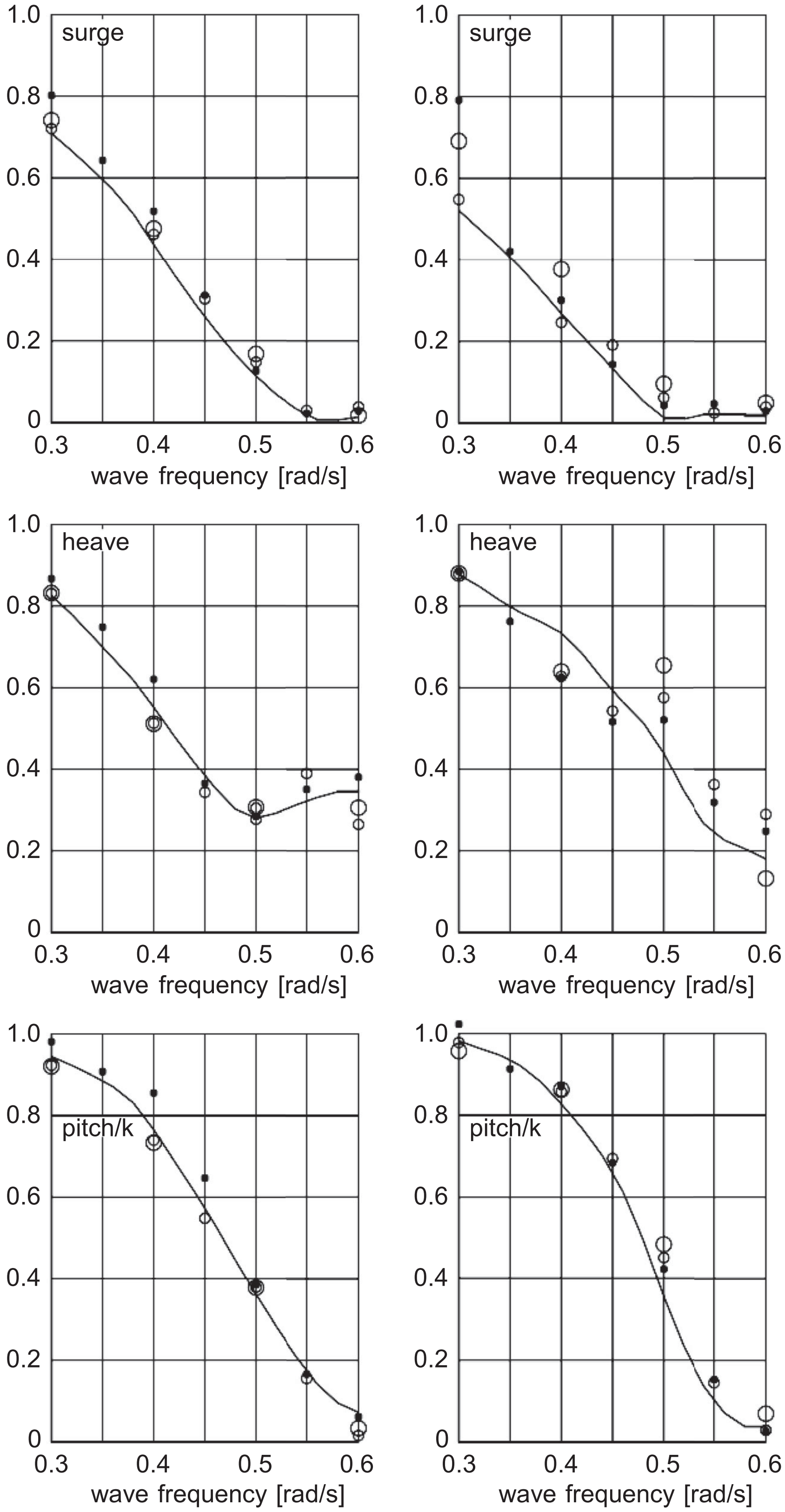

Figure 6. Transfer functions of surge, heave and pitch motion of the 6500 TEU containership at *G* in head waves for speed 5 (left) and 15 (right) knots. Curves: Results of programme GLRankine (Söding et al., 2012); dots: results of model experiments by MOERI; circles: present method for larger and smaller control forces (larger, smaller circles).

hand, results of model experiments and present simulations, and, on the other hand, the linear panel method and the RANSE calculations, deserve further investigation. The same holds for the vertical bending moment transfer functions at high wave frequencies: They appear substantially larger than the results of the other methods, which is in contrast to results for higher wave amplitudes (Figure 8).

Whereas Figures 6 and 7 show results for small wave amplitude, Figure 8 gives results in steep waves

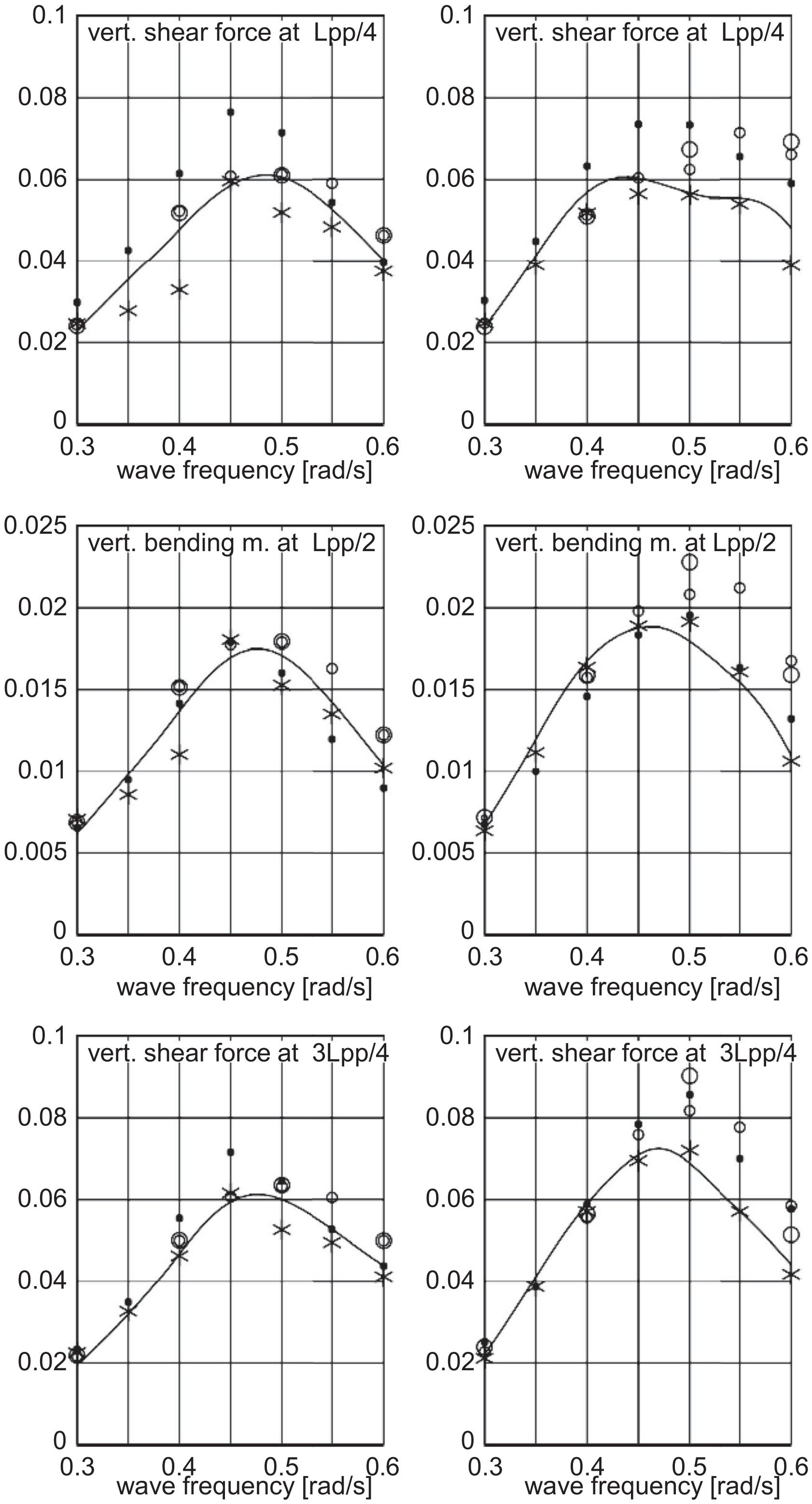

Figure 7. Non-dimensional shear force $F_z/\rho g L_{pp} BA$ at stations in the after- and fore-body, and bending moment $M_y/(\rho g L_{pp}^2 BA)$ (A = wave amplitude) at midship section. Asterisks for RANS calculations (von Graefe et al., 2014). Other details like in Figure 6.

of 7 m (left) and 10m (right) wave height. Here nonlinear effects, especially differences between the absolute value of positive and negative responses, are important. Because these differences are much larger for loads than for motions, here nonlinear section loads are presented. Details of the response evaluation can be important. Because of their relevance for dimensioning the ship structure, non-dimensional values of the maximum and minimum loads within an encounter period (averaged over a few encounter periods) minus the corresponding load without waves, but with forward speed are presented. Various alternative evaluations are possible but appear less relevant, for example, to use the Fourier coefficients of the load's time track at the encounter frequency, or to subtract from the extreme values the average load

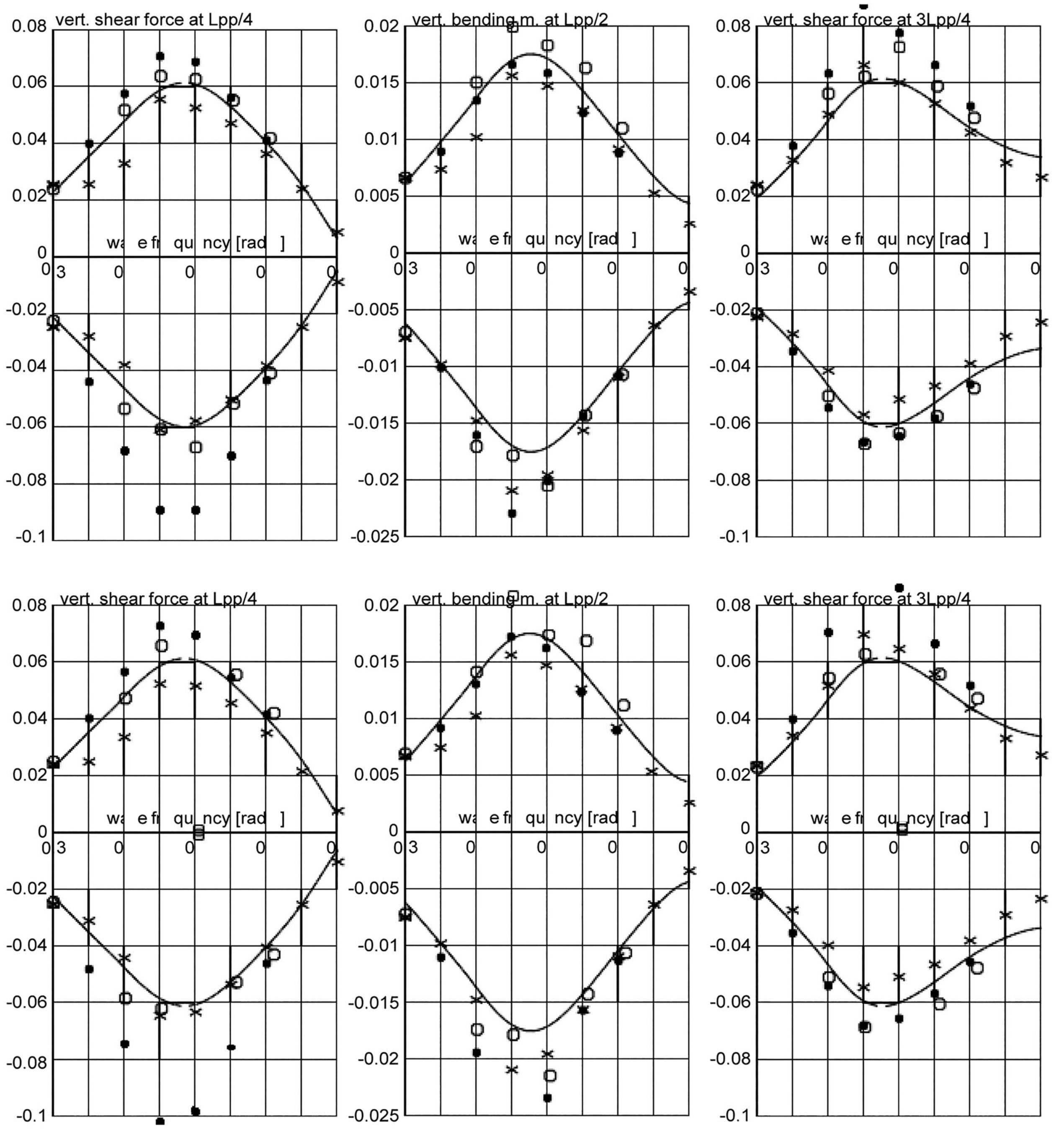

Figure 8. Maximum and minimum non-dimensional shear force $F_z/(\rho g L_{pp} BA)$ and bending moment $M_y/(\rho g L_{pp}^2 BA)$. 6500 TEU containership sailing with five knots in regular head waves of 7 m (left) and 10 m (right) height. Curves: linear programme GLRankine; dots: model experiments by MOERI; asterisks: RANS calculations (Söding et al., 2012); circles: present method.

in still water without speed ahead, or the average load in the wave.

Finally, Figure 9 gives results for another containership, the Duisburg Text Case (DTC), in steep head waves. The figure presents heave and pitch motions and the added resistance coefficient $C_{AR} = R_a/(\rho g \zeta_A^2 B^2/L_{pp})$, where ζ_A is wave amplitude. Results of model experiments are compared with those of RANSE calculations [Sigmund and el Moctar 2018] and of the present method for a coarser and a finer body panel mesh. The wave steepness $2\zeta_A/\lambda$ decreased from 4.5% for $\lambda/L_{pp} = 0.44$ gradually to 1.43% for $\lambda/L_{pp} = 2.50$. The close coincidence of results by different methods for the same wave conditions demonstrates an exceptional accuracy of both the model experiments and the nonlinear calculations.

6. Verification for a rigid ship hull in regular quartering waves

Accurate simulations in quartering waves cause more difficulties than simulations in head or following waves. Reasons for this are:

- Roll eigenperiods are large compared to the eigenperiods of the other degrees of freedom due to the

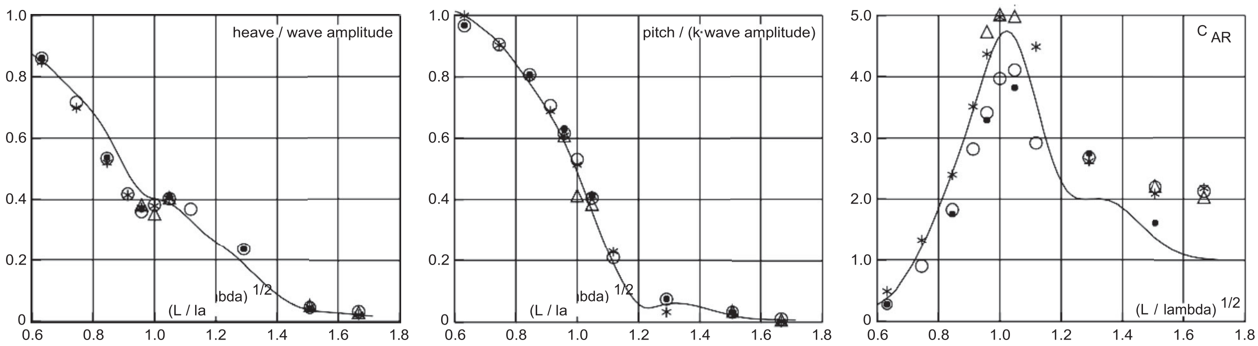

Figure 9. Nondimensional heave and pitch motion and added resistance coefficient of the DTC containership in steep head waves at $F_n = 0.139$. Δ model experiments, * RANSE calculations both from Sigmund and El Moctar (2018); ∘ and • present method for coarse and fine body panel mesh, respectively. The curves show results of the linear programme GLRankine (Söding, Shigunov et al., 2012).

small roll restoring moment. Thus roll motions are sensitive, for example, for control forces in the simulations, or for steering control or spring forces in model experiments.

- Roll restoring is highly variable in waves; it may even become negative on a wave crest.
- Viscous effects are more important for roll, sway and yaw motions than for heave and pitch.

Correspondingly, large differences between measured and computed motions are found for roll motions in long waves (small wave frequency; Figure 10). A small metacentric height GM of only 1.14 m was assumed in experiments (1.8 cm in model scale) and computations. Thus roll motions may have been influenced by the soft springs used in the experiments to keep the model on course.

Contrary to the roll motion, measured and computed linear and nonlinear results agree quite well for the other five kinds of motions. Corresponding results are found for loads: Torsional moments, which are small, sensitive and strongly influenced by roll motions, show large differences between measurements and calculations, whereas bending moments and shear forces agree well, as is shown for the horizontal bending moment in Figure 11.

7. Results for an elastic hull in in regular head waves

This chapter gives results of the present method for the 10,000 TEU ship (Oberhagemann,2016), assuming an elastic hull modelled as a Timoshenko beam. Six

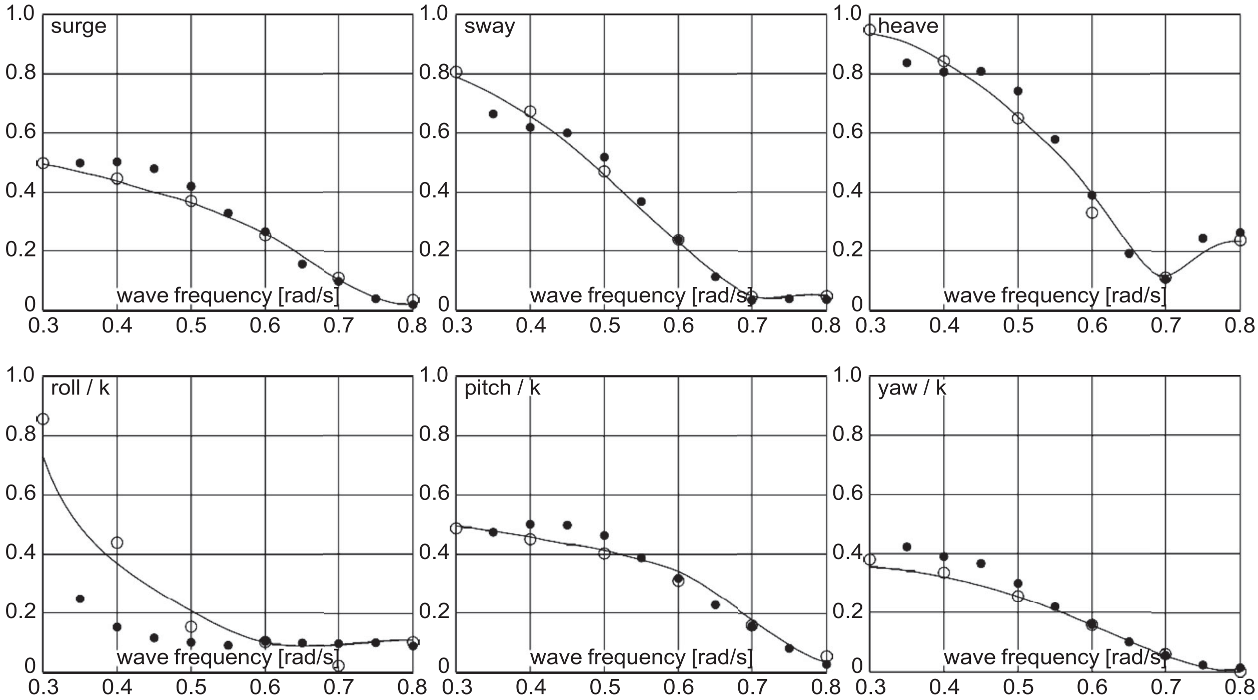

Figure 10. Linear motion transfer functions of the 6500 TEU containership at G in quartering waves ($\mu = 60^\circ$) at speed 5 kn. •: experimental results by MOERI; curves: linear panel method GLRankine; circles: present method.

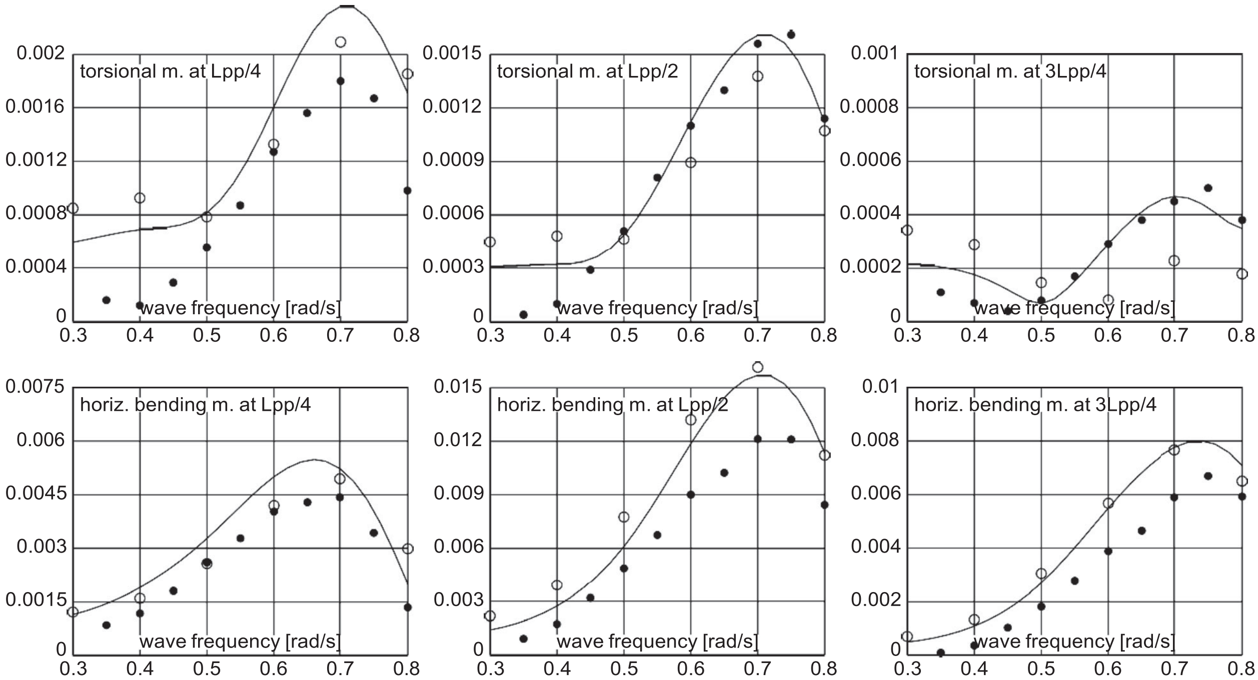

Figure 11. Linear transfer functions of the nondimensional moments $M/(\rho g L_{pp}^2 BA)$ (upper figures torsional, lower horizontal bending moment) at three sections. Other details like in Figure 10.

vertical vibration modes were determined for the hull in still water before starting the simulations. Figure 12 shows time tracks of motions and loads in the midship section. An initial interval is substituted by a straight lines to avoid excessive transient values. Results refer to the ship sailing with 10 knots in regular head waves of 310 m length and 8 m height. In this condition, the wave encounter frequency is 1/5 of the lowest vibration eigenfrequency; thus the 5th order wave excitation is in resonance with the 2-node bending mode. Whereas the centre of gravity motion is not influenced by the vibrations (as it must be), the midship section loads show a superposition of oscillations with the wave encounter frequency and the 2-node vibration eigenfrequency.

Figure 13 shows the same for the time functions v_j in Equation (1) of the lower vibration modes, which correspond to vertical vibrations of the hull structure. Substantial vibrations are excited for the lowest vibration mode because of the above-mentioned resonance condition. The next higher mode oscillates nearly alone with the wave encounter frequency, and the 4-node mode factor shows only a small constant value caused by the still-water bending moment, except for initial vibrations, which occur because the initial hull deformation is assumed as zero.

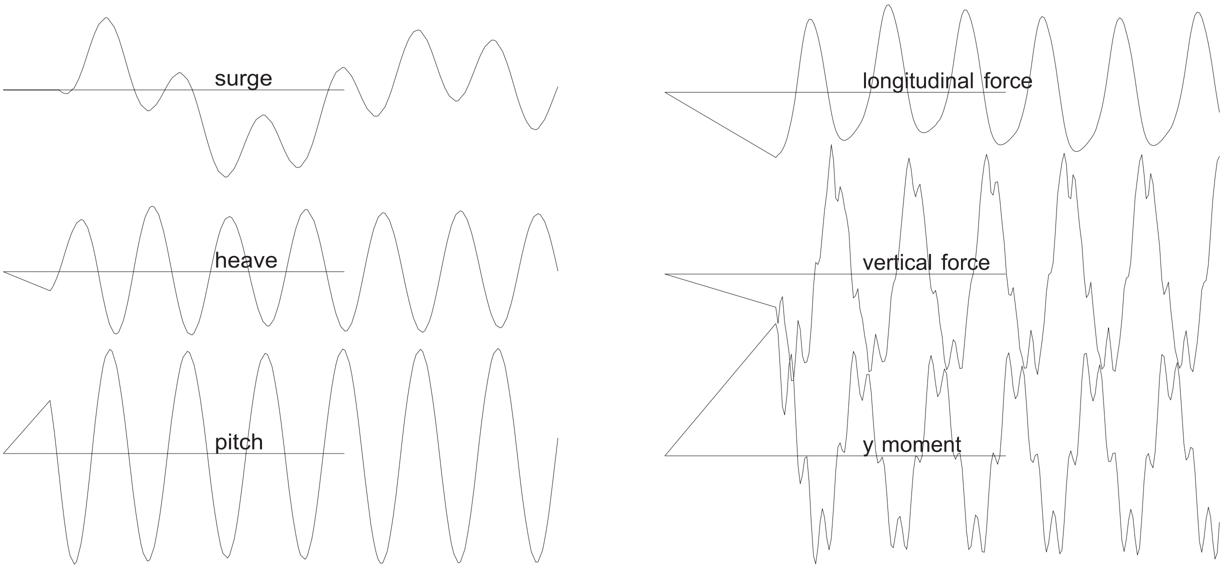

Figure 12. Time function of motions (left) and midship section loads (right) of the elastic 10,000 TEU containership at G in regular head waves of 310 m length and 8 m height. Speed 10 knots.

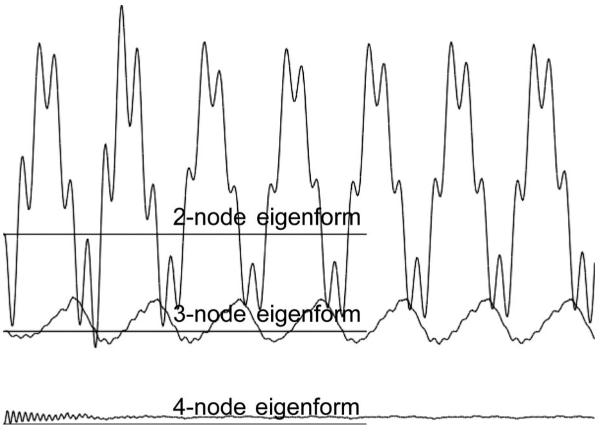

Figure 13. Time function of mode vibrations. Other details like in Figure 12.

Figure 14 shows computed vertical bending moments at midship section in the same ship, again at 10 knots speed in regular head waves, but here for waves of various lengths λ and a wave height of 8m, but (in short waves) not more than $\lambda/30$. The average hogging moment of, roughly, 5 GNm is caused mainly by the still water moment, slightly modified by the steady and the oscillating waves. The broken lines give the average value ± the moment amplitude averaged over a few encounter cycles; the amplitudes result from a Fourier analysis at the wave encounter frequency. The lower and upper continuous lines connect other results of the same simulations: the maximum and minimum moments during an encounter period, again averaged over a few encounter periods. The curves show spikes where the encounter period is near 4 or 5 times the 2-

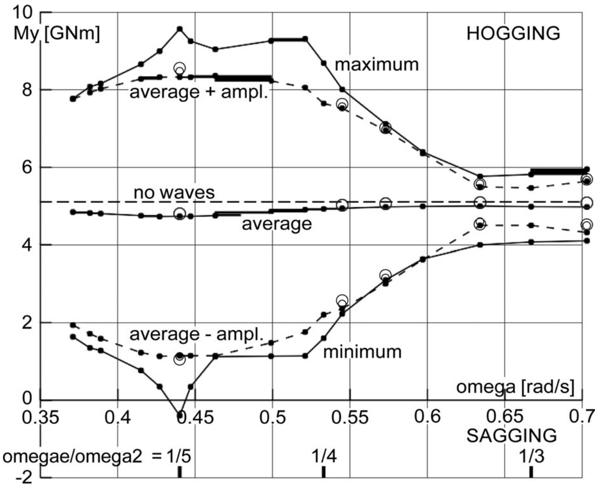

Figure 14. Midship vertical bending moment of the elastic 10 000 TEU containership in regular head waves. Wave height = Min(8 m, wave length/30). Speed 10 knots. $\omega_2 =$ 2-node bending eigenfrequency. Circles for rigid hull: small for average ± amplitude, large circles for extreme loads.

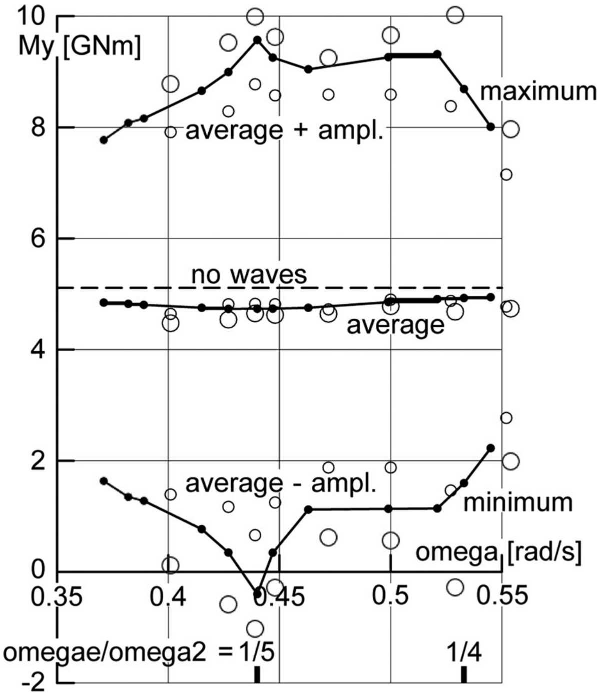

Figure 15. Minimum and maximum midship bending moments like in Figure 14. Additional results for wave heights 7/8 (small circles) and 9/8 (large circles) times Min(8 m, wave length/30).

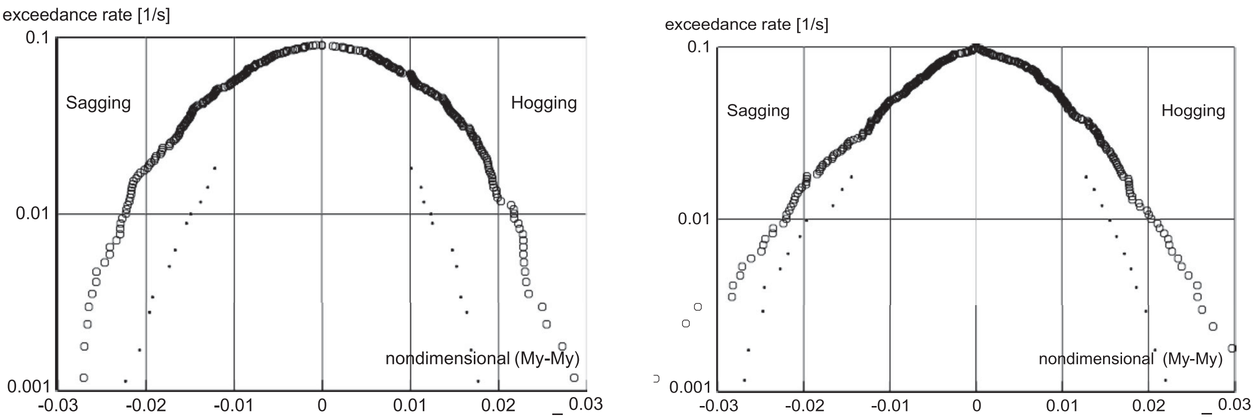

Figure 16. Exceedance rate of extreme nondimensional midship bending moments $M_y/(\rho g B L_{pp}^2 H_s/2)$ for the 10,000 TEU containership sailing with 10 knots speed in a long-crested head sea of JONSWAP spectrum (peak enhancement factor 3.3) of zero-upcrossing period $T_z = 11.5$ s and significant wave height $H_s = 6.5$ m. Left side rigid, right side elastic hull. Circles: present method; dots: comparable results of Oberhagemann (2016).

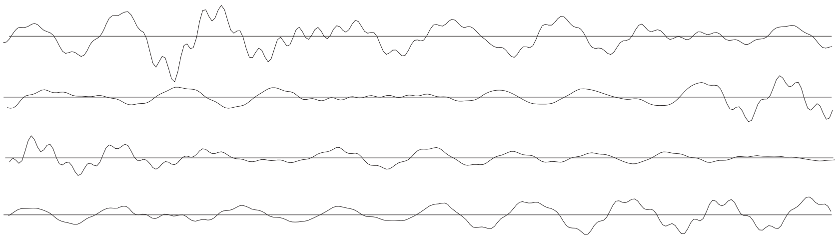

Figure 17. Example time track of midship bending moment. Ship and wave conditions as for Figure 16.

node eigenfrequency (see the scale at the bottom of the figure). These spikes are caused by the 4th or 5th, respectively, order of the vibration excitation.

To further demonstrate the effect of hull elasticity, the circles are results simulated for the rigid hull: small circles give average value ± amplitude, larger circles minimum, average and maximum values during an encounter period. The results show:

- For a rigid hull, the moment varies so smoothly that there is nearly no difference between extreme values and average value ± Fourier amplitude for the encounter frequency.
- Average values ± Fourier amplitudes for the encounter frequency are practically identical for the rigid and the elastic hull.
- Averaged over the relevant frequencies, both maximum moments and moment ranges, which cause fatigue damage of the structure, are substantially larger in the elastic than in the rigid hull.

Normally the exciting regular waves are computed including nonlinear effects by using Fenton's method up to order 20. Alternatively, linear Airy waves were used in simulations for the elastic hull. For all frequencies, the results were nearly identical, showing that higher order effects (especially vibration excitations) are nearly alone caused by nonlinear responses of the hull, not by the nonlinearity of the waves.

From perturbation theory one would expect that the 5th order excitation amplitude, and in case of linear damping also the vibration amplitude at 5th order resonance, would increase with the 5th power of the wave amplitude. This was tested by using 7 m and 9 m wave amplitude instead of the 8m used in Figure 14. Figure 15 shows the result: Near to the 5th order resonance frequency the difference between extreme and average non-dimensional moment is, approximately, proportional to the wave amplitude raised to the power of 1.4 in sagging, and 1.2 in hogging. Reasons for the deviation from perturbation theory are:

- At the 5th order resonance, a large part of the bending moment is caused not by the vibration, but by oscillations with the wave encounter frequency.
- Perturbation theory is valid only in the limit of low wave amplitude.

Figure 15 shows further that, for frequencies near the 4th order resonance, the difference between extreme and average bending moment is proportional to the wave amplitude raised to the power of about 1.6 both in hogging and sagging.

8. Results in natural seaway

It was tried to compare simulations in a natural seaway using the present method with results published by other authors. However, results for a time interval which allows a meaningful statistical evaluation are

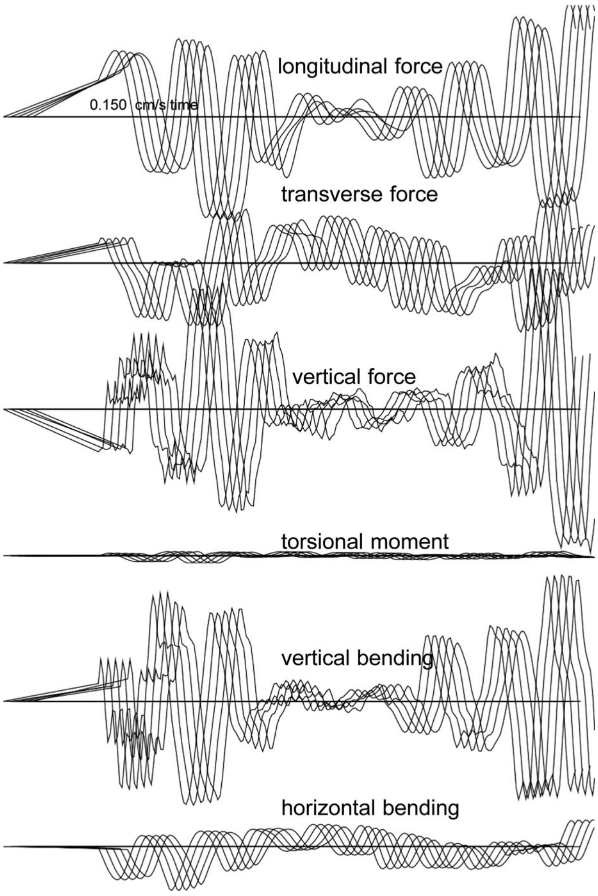

Figure 18. 10 000TEU containership in short-crested JONSWAP head seaway $H_s = 7$m, $T_1 = 12$s. Time tracks of midship section force and moment shifted horizontally depending on peak wave length over free surface panel length = 30, 25, 20, 15, 12.

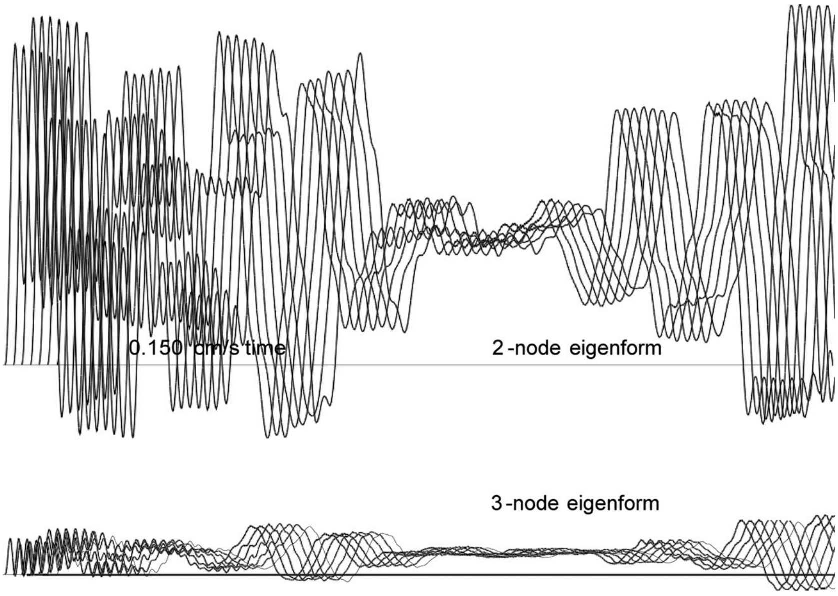

Figure 19. Ship and waves like in Figure 18. Time tracks of modal vibrations shifted horizontally depending on peak encounter period over Runge–Kutta time step = 39, 33, 28, 22, 19, 16, 12.

scarce, because such simulations (of $>=$ 30 minutes duration) take very much computer time when using the usual CFD methods. Results by Oberhagemann (2016) were found most suitable for a comparison, especially his simulations of the elastic hull of the 10 000TEU containership in a head long-crested JONSWAP (peak enhancement factor 3.3) seaway of zero-upcrossing period $T_z = 11.5\,\mathrm{s}$ and significant wave height $H_s = 8.5\,\mathrm{m}$. However, it turned out that, in this condition at the prescribed speed of 10 knots, the ship's deck was repeatedly flooded. In this condition the present method fails because the waterline becomes rugged; the method tolerates deck flooding only in case of large heel angles. To avoid deck flooding, H_s had to be reduced to 6.5 m. The result is shown in Figure 16 for the rigid (left) and for the elastic ship hull (right). Between each pair of successive upcrossing events of the mean value of the midship vertical bending moment, only the minimum and the maximum moment were plotted as small circles. The ordinates give the exceedance rate found in a simulation of 30 min duration.

The dots in Figure 16 show roughly corresponding results of [Oberhagemann 2016], however for $H_s = 8.5\,\mathrm{m}$. The non-dimensional bending moments would be independent from wave height in case of linear responses. However, nonlinear effects cause an increase of the nondimensional bending moment with wave height in case of no deck submergence (see Figure 5), and a decline in case of substantial deck flooding. Further, differences of evaluation contribute to the large differences between dots and circles:

- The dots in the left diagram were computed not for the rigid hull, but result from the low-pass filtered response of the elastic hull.
- (Oberhagemann,2016) determined extreme values between upcrossings of the average value by the low-pass filtered time tracks, both for the left and the right diagram.

For the simulation used to construct the right diagram of Figure 16, Figure 17 shows part of the time track of the midship vertical bending moment of the elastic hull. It contains a mixture of whipping (suddenly excited) and springing (continuously excited) hull vibrations (higher-frequency oscillations) between intervals of nearly no vibrations.

Simulations in a natural seaway are well suited to investigate the effect of various numerical parameters on the results, simultaneously for elementary waves of various frequency and directions. As examples, Figure 18 demonstrates the effect of the free-surface panel size on section force and moment, and Figure 19 the effect of the time step size on modal vibrations.

9. Conclusions

A method to simulate nonlinear ship motions and loads in steep waves is presented. Compared to the usually applied RANSE methods, it needs less computing effort by orders of magnitude. This is accomplished by using a fully nonlinear potential method to determine fluid force and moment. Compared to RANSE methods, the disadvantage is that the method fails if substantial parts of the deck become submerged while the heel angle is small. In that case, the structured panel mesh on the free surface contains extremely distorted panels, which are nearly parallel to body panels on the deck. Both facts lead to instability of the method.

The present method has been developed during about a decade and is now mature, giving accurate results both in regular waves and presumably (because good comparison data are lacking) also in natural seaways, both for rigid and elastic ship hulls.

The source code of the method is available from the author if an adequate gift is donated to the Médecins Sans Frontières.

Disclosure statement

There is no potential conflict of interest. The research did not receive any specific grant from funding agencies.

ORCID

Heinrich Söding http://orcid.org/0000-0002-1822-0859

References

Bandyk PJ, Beck RF. 2011. The acceleration potential in fluid-body interaction problems. J Eng Math. 70 (1-3):147–163.

Bertram V. 1990. Ship motions by a rankine source method. Schiffstechnik. 374:143–152.

Bertram V, Söding H, Graf K. 2006. PDSTRIP – a strip method for ship and yacht seakeeping. 8th NuTTS, Nantes.

Brix J (ed). 1993. Manoeuvring technical manual. Hamburg: Seehafenverlag.

Dawson CW. 1977. A practical computer method for solving ship-Wave problems. In: Proc. 2nd Int. Conf. on Numerical Ship Hydrodynamics, Berkeley; p. 30–38.

Ducrozet G, Bonnefoy F, Le Touze D, Ferrant P. 2016. HOS-ocean: open-source solver for nonlinear waves in open ocean based on high-order spectral method. Comput Phys Commun. 203:245–254.

El Moctar BO, Schellin TE, Söding H (2021). Numerical methods for seakeeping problems. Cham: Springer.

Fenton JD. 2018. Use of the programs Fourier, Cnoidal and Stokes for steady waves. Available from: http://johndfenton.com.

Ferziger JH, Peric M (2008). Computational methods for fluid dynamics. Berlin: Springer.

Hachmann D. 1986. Determination of the wave elevation at ship sections based on pressure variations at the design waterline under the influence of the Smith effect, Technical Report MTK325 II, Germanischer Lloyd Hamburg.

Hachmann D. 1991. Calculation of pressures on a ship's hull in waves. Ship Techn Res. 38:111–133.

Hong SY. 2013. Wave induced loads on ships, Joint industry project III. Technical Report No. BSPIS7230-10306-6. Available from: MOERI, Daejeon.

Korvin-Kroukovski BV, Jacobs W-R. 1957. Pitching and heaving motions of a ship in regular waves, Tr.SNAME Vol. 65, p. 590–632.

Mathisen J, Storhaug G, Heggelund SE. 2009. Whipping vibrations in bending stresses measured under harsh stationary conditions. Temarel P and Hirdaris S, editors. In: 'Hydroelasticity in Marine Technology'; ISBN 9780854329045.

Mola A, Heltai L, DeSimone A. 2017. Wet and dry transom stern treatment for unsteady and nonlinear potential flow model for naval hydrodynamics simulations. J Ship Res. 61(01):1–14.

Oberhagemann J. 2016. On prediction of wave-induced loads and vibration of ship structures with finite volume fluid dynamic methods, [dissertation]. University Duisburg-Essen. 201.

Papanikolaou A, Schellin TE. 1992. A three-dimensional panel method for motions and loads with forward speed. Ship Technol Res. 39(4):147–156.

Sigmund S, El Moctar O. 2018. Numerical and experimental investigation of added resistance of different ship types in short and long waves. Ocean Eng. 147:51–67.

Söding H. 1993. A method for accurate force calculations in potential flow. Ship Technol Res. 40:1760–186.

Söding H. 2001. How to integrate free motions of solids in fluids. Proc. NuTTS.

Söding H. 2009. Computation of springing transfer functions, Proc. IMechI: Vol. 223 Part M: JEME Vol. 158, p. 291–304.

Söding H. 2020. Fast accurate seakeeping predictions. Ship Techn Res. 67(3):121–135.

Söding H, Shigunov V, Schellin TE, El Moctar O. 2012. A Rankine panel method for added resistance of ships in waves, OMAE, jn2/OMAE2012-83457.

Söding H, von Graefe A, Moctar O, Shigunov V. 2012. Rankine source method for seakeeping predictions, OMAE, paper 83450.

van Walree F, Serani A, Diez M, Stern F. 2020, October. Prediction of heavy weather seakeeping of a destroyer hull form by means of time domain panel and CFD codes, 33rd Symp. on Naval Hydrod., Osaka.

von Graefe A, Oberhagemann J, Shigunov V. 2014. Linear and nonlinear sectional loads with potential and field methods. J OMAE. 136:031602.